

Review

Surface Potential/Charge Sensing Techniques and Applications

Songyue Chen , Hepeng Dong  and Jing Yang

Department of Mechanical and Electrical Engineering, Xiamen University, Xiamen 361005, China; 19920171150927@stu.xmu.edu.cn (H.D.); jingyang@stu.xmu.edu.cn (J.Y.)

* Correspondence: s.chen@xmu.edu.cn; Tel.: +86-138-6048-7347

Received: 5 February 2020; Accepted: 15 March 2020; Published: 18 March 2020



Abstract: Surface potential and surface charge sensing techniques have attracted a wide range of research interest in recent decades. With the development and optimization of detection technologies, especially nanosensors, new mechanisms and techniques are emerging. This review discusses various surface potential sensing techniques, including Kelvin probe force microscopy and chemical field-effect transistor sensors for surface potential sensing, nanopore sensors for surface charge sensing, zeta potentiometer and optical detection technologies for zeta potential detection, for applications in material property, metal ion and molecule studies. The mechanisms and optimization methods for each method are discussed and summarized, with the aim of providing a comprehensive overview of different techniques and experimental guidance for applications in surface potential-based detection.

Keywords: surface potential; surface charge; nanowire; nanopore; zeta potential

1. Introduction

Surface potential sensing techniques measure the surface charge density over the solid surface or solid–liquid interface. Most recent developments in sensing techniques focus on the latter situation due to the difficulties associated in charge detection in liquid. The surface potential over the solid–liquid interface is vital for a variety of physicochemical related applications, such as chemical, engineering, biological, and even production processes, including sensing [1–3], catalysis [4], corrosion prevention [5], cell adhesion and aging study [6,7], nanoparticle separating [8], pulp toughness [9] and so on. In the presence of an electrical double layer (EDL) when immersing solid into liquids, the target chemical or biological inputs are transformed into electrical signals, referred as surface potential or surface charge. Surface potential ϕ_o has a linear relationship with surface charge density as $\sigma = C_{dl}\phi_o$, where C_{dl} is the double layer capacitance that is determined by the ionic strength and ionic valence. Surface potential can be modulated by adsorption of target molecules, e.g., chemical concentrations (pH [10–12], metal ion concentration [13,14], etc.), biological species (DNA [15–17], protein [18], etc.), electrical modulation (reference electrode) and physical movement (flow velocity [19,20]). In other words, those variables that induce potential or charge change can be detected through surface potential or charge measurement.

In this review, surface potential/charge detecting methods are categorized into three groups for characterizing macroscopic surface and/or micro/nano particles (as shown in Figure 1): direct potential measurement with Kelvin probe force microscopy and chemical field-effect transistors (chemFETs), surface charge measurements with nanopore sensors, and zeta potential measurements with streaming potential measurements and optical detection techniques.

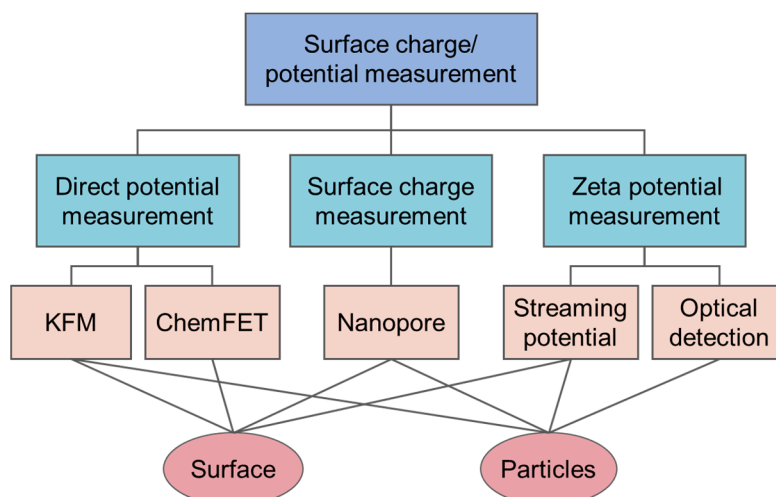


Figure 1. Surface charge/potential measurement techniques.

2. Direct Surface Potential Measurement

2.1. Kelvin Probe Force Microscopy (KFM)

Kelvin probe force microscopy (KFM) is a tool that can perform nanoscale imaging of surface potential for a variety of materials [21] at a sub-nanometer resolution [22]. It is an atomic force microscope (AFM)-based instrument that measures the contact potential difference (CPD) between the sample surface and the tip, with $V_{\text{CPD}} = (\varphi_{\text{tip}} - \varphi_{\text{sample}})/e$, where φ_{tip} and φ_{sample} are the work functions of the tip and the sample, respectively, and e is the elementary charge. When the AFM tip approaches the sample surface, electrical potential is generated due to the difference in Fermi levels. In 1991, Nonnenmacher initiated the technology for measuring the contact potential between different metal materials [21]. Thereafter, KFM has been widely used to characterize the localized surface potential of metals, semiconductors [23–25], TiO_2 [26], organic materials [27,28], biomaterials [29] in polar liquids and, recently, in non-polar solutions as well [30]. There are two main operation modes: oscillation amplitude modulation (AM) mode and oscillation frequency modulation (FM) mode [22]. AM mode measures the direct force between the tip and sample [31]; FM mode detects the force gradient [32], which gives a higher spatial resolution. The AM mode has a spatial resolution of, typically, 25 nm and a potential resolution of 5 mV [22]. The FM mode can reach sub-nanometer resolution and has a potential resolution of 10–20 mV [22].

KFM is commonly used for solid surface inspection. When combined with an optical fiber probe, the photoexcitation effect on surface potential of Alq_3 thin films can be measured [33]. Stone et al. [30] demonstrated qualitative estimation of fibril surface charge with different functional chemical groups after exposure to water through potential measurement by KFM (Figure 2a). Cohen et al. [34] obtained potential measurements for metal contacts on SiO_2 and showed the effect of voltage bias, as shown in Figure 2b.

Besides solid and wet surfaces, KFM are also applied in ion and biomolecule detection with localized surface chemistry design. Park et al. [35] demonstrated the precise recognition of biomolecule interaction with KFM, which can quantitatively describe single-molecule interactions, such as protein kinase–ATP interactions, as shown in Figure 2c. Jang et al. [36] reported a highly sensitive mutation detection with a gold nanoparticle (AuNP)-based platform (Figure 2d) by evaluating the surface potential change of each AuNP on silicon substrate, during probe DNA modification and target DNA hybridization, with a detection limit of 3.3 pM. Leung et al. [37] showed the single-molecule detection of avidin molecules and DNA, with a resolution of five basic amino acids. They based the expected charge pattern measurements on individual DNA molecules and proteins after further refinements. The metal ion detection is based on the surface potential change at ionic adsorption, e.g., Hg^{2+} ion

detection by formation of thymine–Hg²⁺–thymine at a detection limit of 2 fmol [38], Ag⁺ ion detection by formation of cytosine–Ag⁺–cytosine at a detection limit of 20 fmol, as schematically shown in Figure 2e [39], and Al³⁺ ion detection by exposure to citrated AuNPs at a detection limit of 2 amol, as shown in Figure 2f [40]. The material difference between the substrate and nanoparticles favors specific surface chemistry for potential measurements—e.g., thiol chemistry works on Au, but not on silicon substrate.

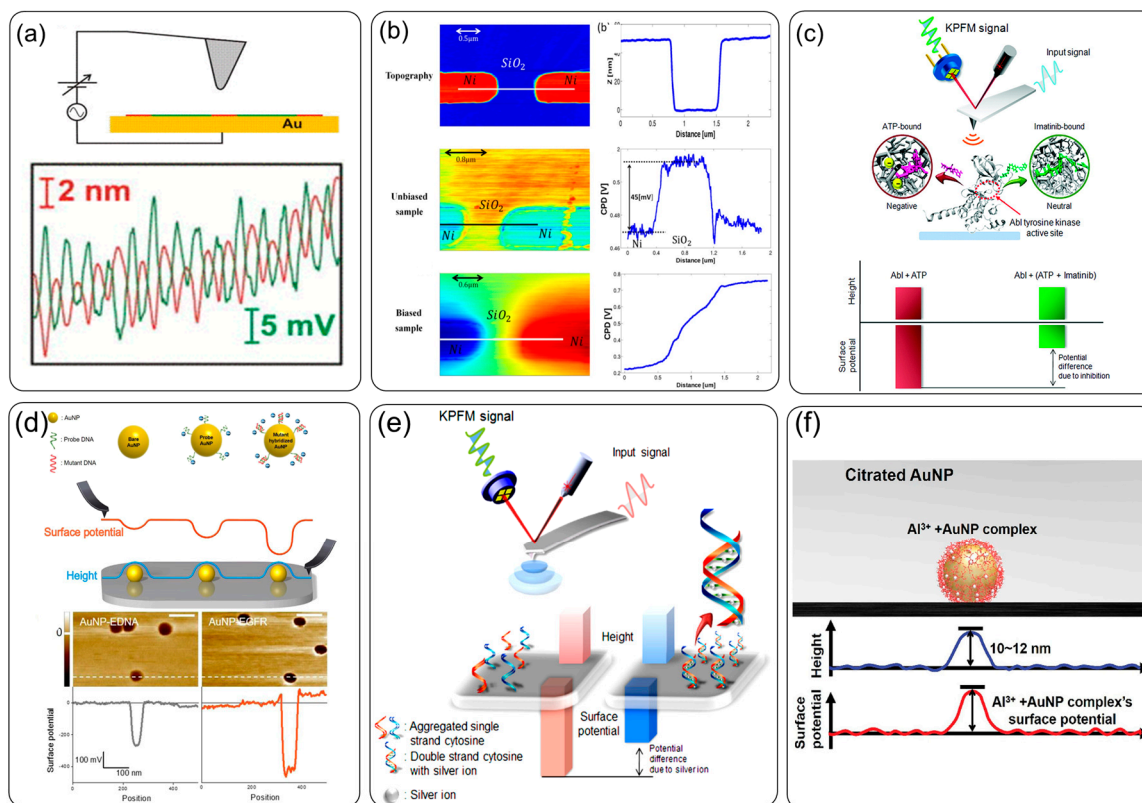


Figure 2. Kelvin probe force microscopy (KFM) for surface potential images: (a) schematic diagram of the detection in air (top graph), and in the bottom graph, the red line represents the topography for fibril, and the green line represents the surface potential [30]; (b) the morphology and contact potential difference for metal contacts on SiO₂ surface for unbiased and biased sample [34]; (c) recognition of single-molecule interaction between protein and small ligands [35]; (d) DNA on a gold nanoparticle (AuNP) for mutation study by comparing the height and surface potential signals [36]; (e) single-molecule detection of avidin molecules and DNA [37]; (f) Al³⁺ ion detection on citrated AuNPs [40].

Compared to other measurement techniques, KFM has excellent spatial resolution and relatively high potential sensitivity. However, measurement of the absolute surface potential using KFM needs a reference work function, which requires the calibration of the KFM probes [41]. Performing the necessary exchange of the two samples under the KFM probe will reduce the accuracy of the measurement [41]. When measuring a surface, KFM can only measure changes in the average surface potential of the molecule. Sudden changes in terrain height reduce the accuracy [22,42]. Besides, the time cost for such a measurement is high and the measurements can only work in non-conducting environments. More recently, another AFM-based potential detection technique was developed for electrostatic force imaging by analyzing the resonant frequencies. Specifically, electrostatic force microscopy operated in multifrequency mode, provides a promising technique for improving the spatial resolution and time resolution [43], and can be applied to obtain electrostatic and topographic images simultaneously [44,45].

2.2. Chemical Field Effect Transistor (ChemFET)-Based Potential Sensing

When a chemFET is immersed in an electrolyte, the electrostatic gating through the liquid and gate dielectric layer, generally named liquid-gating, modifies the carrier mobility in the transistor, as illustrated in Figure 3a. When the surface charge density on the gate changes, the surface potential can be measured by the device conductivity change. Materials for such FET devices include semiconductors, e.g., ion sensitive field effect transistor (ISFET) and Si nanowires (NWs) [12,46], nano ribbon [18,47], carbon nanotubes (CNTs) [15,48], and graphene [1,10,49].

The surface potential change induced conductivity change is generally monitored through a constant current mode [50], which is commonly used for ISFET, a constant voltage mode [12,51], a threshold voltage shift scan [15,52,53], the ion-step method [14,54], or a Dirac voltage shift scan (for graphene [55,56]). A constant current mode is generally used in ISFET where the current value is relatively high, and a feedback voltage is applied to the gate voltage to maintain a constant current in the transistor. The change in feedback voltage is therefore regarded as the surface potential change. A constant voltage mode is mainly used in nanostructured field effect transistors (nanofETs), e.g., NW, CNT, Graphene, where the current is generally small and the surface potential induced conductivity change is monitored by electric current. Threshold voltage scan can be applied in most device conditions by applying a scanning of gate voltage and finding a threshold voltage recording to the characteristics of the gate voltage-current curve. For graphene, the corresponding variable is Dirac voltage, where there are equal amounts of electrons and holes. Ion-step method is a stimulus-response method that is less sensitive to drift [14]. An ion-step from low to high ionic strength solution is applied to the gate oxide. A sudden increase of double layer capacitance C_{dl} is expected and a change in current can be measured due to the reduction in surface potential, since $\phi_o = \sigma_o/C_{dl}$, where σ_o is the surface charge density.

ChemFETs, especially nanofETs, for surface potential detection are applied extensively in different fields. ISFET sensors were initially designed based on the proton sensitivity of the gate oxide–electrolyte interface, and later for membrane-covered ISFETs for various types of target detection [57,58], e.g., charged protein sensing with an immobilized antibody [59] or detection of proton release from protein phosphorylation by catalysis [60]. The development of nanofET brought FET sensors higher spatial resolution and sensitivity. Si NW biosensors are used for DNA detection and they can achieve a 1fM level by enhancing the signal with rolling circle amplification [61]. The Dekker's group demonstrated a probed DNA translocation event with a graphene nanoribbon where a nanopore was also fabricated [62]. Both their nanoribbon and nanopore current signals are recorded for comparison (Figure 3b). They can be used to construct a localized probe for extracellular and intracellular biochemical potential measurements [63–65]. The Lieber group detected extracellular neuronal signals with high-density NW arrays [64], as shown in Figure 3c, which can measure the rate, amplitude, and shape of potential signal propagation along single axons and dendrites. They later fabricated a kinked Si NW for intracellular potential recordings after modification with phospholipid bilayers (Figure 3d) [65]. Besides, the fabrication process for ChemFETs is amenable to minimization and integration. NanofETs allow array fabrication for the multiplexed sensing of biomolecules [66] and gas compositions [67], which are performed at the chip level. Zheng et al. designed a real-time multiplexed electrical detection of four different cancer protein markers in serum samples [66]. Zou et al. decorated the NW surface with three different metal nanoparticles [67], Au, Ag and Pt, which allow the simultaneous detection of CO, C₂H₅OH, and H₂.

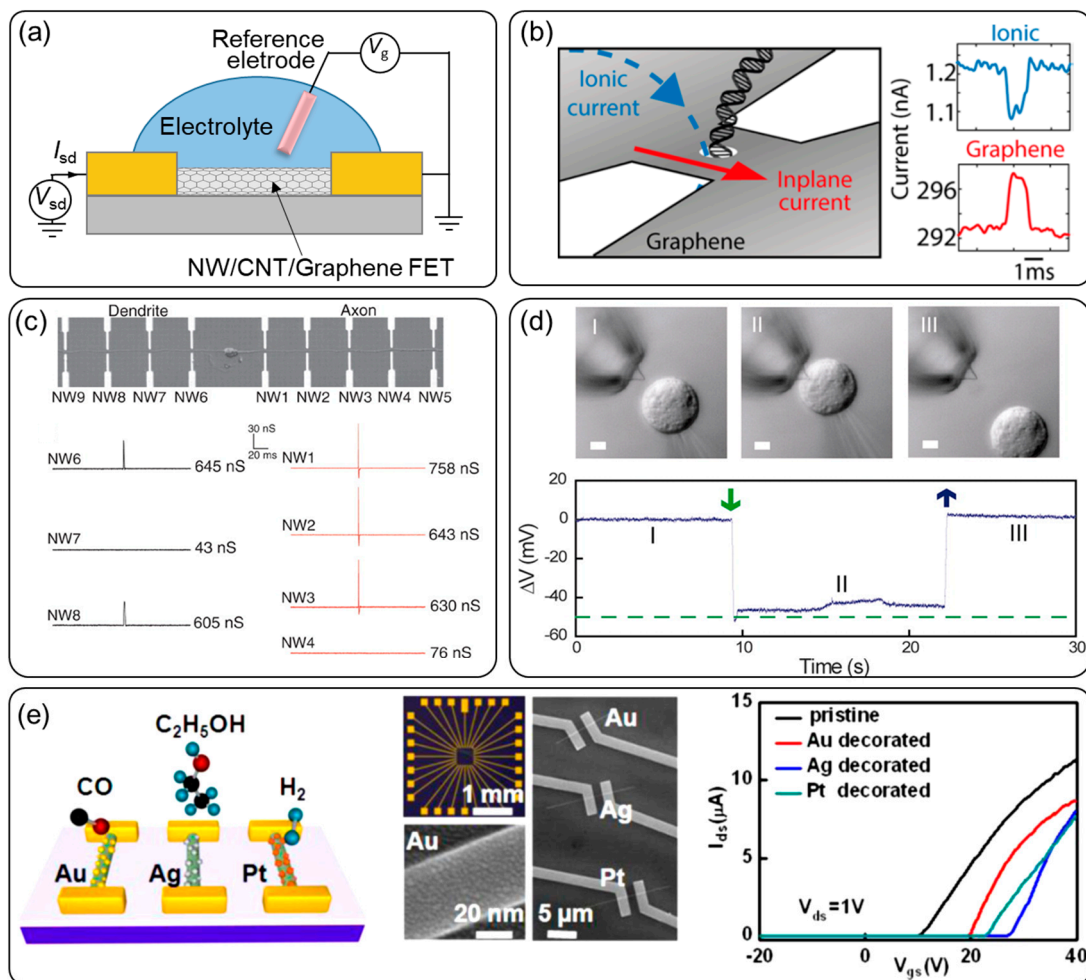


Figure 3. NanoFET configuration and applications: (a) schematic configuration of NanoFETs, (b) DNA translocation event detection with a graphene nanoribbon and a nanopore simultaneously [62], (c) extracellular neuronal signal detection with high-density nanowire arrays [64], (d) intracellular potentials recording with a Si NWs [65], (e) Si NW arrays for gas composition sensing [67].

The surface potential sensitivity of chemFET can be modulated by a few parameters, including the fabrication parameters (e.g., doping, size) [68,69], device operation [52,70], the interface material [51,71], electrolyte ionic strength [72], surface chemistry [73], etc. Doping and size have a significant impact on the charge sensitivity. The reduction in size gives nanoFETs very large surface-to-volume ratio and makes them extremely sensitive to the surface properties. Moreover, Park et al. [74] demonstrated that, by decreasing the impurity doping concentration, the sensitivity increased greatly compared to reducing the device diameter. At the operation level, the tuning of the device in the depletion region and at a higher frequency (e.g., 30 Hz input voltage compared with DC voltage) can optimize the signal-to-noise ratio and the limit of detection [75]. By coupling the back gate with the liquid gate [76], the signal-to-noise ratio in both subthreshold regimes and above-threshold regimes can be improved.

Interface materials with improved dielectric property increase sensitivity. Chen et al. [51] deposited Al_2O_3 gate oxide on Si NWs with atomic layer deposition, and showed near-Nernstian pH sensitivity and superior repeatability. Bashir et al. [71] added a layer of high-k hafnium oxide, to reduce the dielectric thickness and the leakage current, and demonstrated an improved biomolecule sensitivity. Additionally, properly designed surface chemistry, e.g., with additional polyethylene glycol modification, extends the Debye length, and therefore increases the sensitivity of NW sensors in high ionic strength solutions [77]. Masood et al. [78] selectively functionalized alkenyl monolayers on the silicon surface with a carbon–silicon alkyl, which not only reduced the gate thickness, but also

eliminated the fixed oxide charge, and showed dramatic improvements in the device performance and detection sensitivity. By controlling distance of the surface charge layer to the sensor surface through molecular engineering [79] or by bringing the probe in closer proximity to the sensor surface through probe size reduction [80], the device sensitivity can be modulated. The field effect gets stronger when the charged target molecular layer moves closer. Park et al. [59] reported an interfacial charge regulation method by protein-blocking layers on ISFET for direct measurements in serum. Bhattacharyya et al. [81] proposed a local electrostatic method to tune the Debye length, forcing the double layer ion concentration to match the bulk.

3. Surface Charge Measurement

The surface charge measurement in liquid can be realized with solid-state nanopore sensors, including polymer nanopores and inorganic nanopores or nanochannels [2]. Nanopores take advantage of the electrostatic effects inside nano-confined space in the presence of surface charges, which gives them high sensitivity and new sensing mechanisms [82]. The change in surface charge regulates the ionic conductance of nanopores through pH [83], divalent cations and anions [84], ionic concentrations [85], temperature [86], surface chemistry and biomolecules [87], gas [88], salt gradient and voltage polarity [13], and can be characterized by the current–voltage (I – V) curve due to the conductance change that is related to the inner wall surface charge regulation, or the instant current change related to the passing of charged particles through nanopores. The non-uniform distribution of surface charge inside the nanopore greatly affects the current rectification ratio. One of the required condition for surface charge detection is low background ionic concentrations [82,89] in order to minimize the conductance contribution from bulk ions. Since the nanopore diameter has a large influence on the sensitivity [82], smaller nanopores favor charge detection that benefits from electric double layer overlap.

For inner wall surface-based charge regulation, the stimulus from the solution that caused the charge change alters the I – V curve characteristics. By designing proper surface chemistry, metal ion concentrations can be measured through the current rectification ratio, e.g., crown ethers chemistry for the specific adsorption of K^+ ions (Figure 4a) [90], macrocyclic dioxotetraamine derivative functionalization for Hg^{2+} ion determination at a level of 10 pM (Figure 4b) [91], and polyglutamic acid for repeatable Cu^{2+} ion sensing [92]. The adsorption of positively charged metal ions increases the positive charge and, therefore, changes the current rectification ratio. Taking advantage of the biomolecule recognition reaction, e.g., DNA–peptide nucleic acid (PNA), nanopores are used for the sequence specific detection of single-stranded DNA, as shown in Figure 4c [93]. The signal was enhanced by diminishing the channel surface charge with uncharged PNA probes. The hybridization of DNA molecules to the probes increased the negative surface charge. A glass nanopore-based aptasensor was used for lysozyme detection with a sub-pM detection limit [94]. In addition, nanopore sensors can monitor the mobility of charged particles. Figure 4e shows the recognition of different heavy metal ions by monitoring particle velocity while passing an aptamer through the nanopores [95].

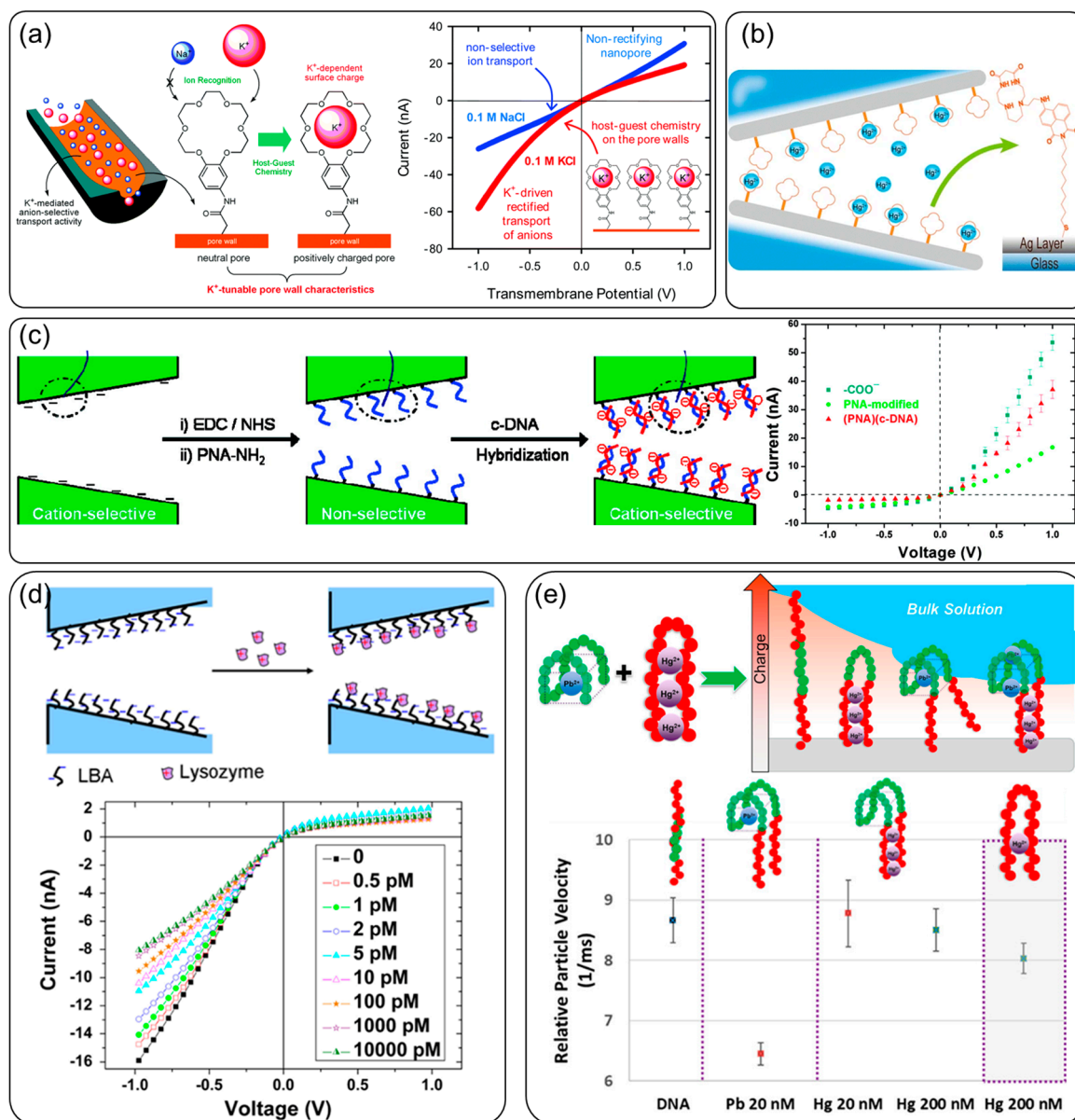


Figure 4. Nanopores for surface charge detection: (a) crown ethers chemistry for specific adsorption of K^+ ions and the current rectification change [90]; (b) macrocyclic dioxotetraamine derivative functionalization for Hg^{2+} ion determination [91]; (c) DNA detection based on PNA–DNA recognition, and the current–voltage (I – V) curve change [93]; (d) lysozyme detection with aptasensor [94]; (e) charged particle detection based on aptamer velocity difference for different heavy metal ions [95].

Although there is a broad amount of research attention paid to solid-state nanopore sensors, there are still remaining questions for the surface charge regulation mechanism inside nanopores and limited applications for stable and repeatable sensing. It is known that there is a significant deviation in pH inside the nanopore from the bulk [96]; however, the regulation mechanism is not clear while performing surface chemistries. Furthermore, the addition of buffer solution also has a significant influence on the charge sensitivity at a low salt concentration and pH [97]. More importantly, the relationship between the surface charge and the I – V characteristics of the nanopore is not yet clear and is difficult to obtain. Therefore, this calls for a systematic understanding of surface charge sensing inside confined spaces.

4. Zeta Potential Measurement

Zeta potential is the electric potential of the slipping plane in the electric double layer with the moving of liquid or solid particles, and is related to the surface charge [98,99]. It is an important parameter describing the behavior of the solid–liquid interface charge, it is affected by solid material properties and liquid phases [100,101], and it represents the key physicochemical surface properties in various fields from electrochemistry to pharmaceuticals [99,102,103]. The zeta potential measurement of a solid wall in solution depends on the streaming potential or electroosmotic mobility measurement technique [104]. For colloids or nanoparticles in suspension, zeta potential is a very important parameter, which is closely related to suspension stability and particle surface morphology. Therefore, zeta potential measurement is widely used in product stability studies and surface adsorption studies [105].

4.1. Streaming Potential Measurement

Flow potential technology has been widely used in planar polymer and glass surfaces to study the electrical properties of solid–liquid interfaces in parallel plate microchannels [106]. For steady incompressible and laminar flow, the streaming potential E_s can be related to the ζ -potential via [107]:

$$\frac{E_s}{\Delta P} = \frac{\varepsilon_r \varepsilon_0 \zeta}{\mu} \frac{1}{(\lambda_b + 2\lambda_s/h)} \quad (1)$$

where ΔP is the pressure difference, h is the channel height, λ_b is the bulk conductivity, and λ_s is the surface conductivity [107]. In order to get a measurable streaming potential, a low bulk conductivity is required, which means a low ionic strength liquid. The detection mechanism is schematically shown in the top image of Figure 5a.

Streaming potential or current measurement has been widely used to characterize charged bulk materials or particles, e.g., biospecific interaction study [108], inorganic material surfaces [109], membranes [110], wood [111], natural and man-made fibers [112], and colloid particles [113]. The bottom image of Figure 5a shows surface treatments, e.g., etching and oxidation, had a profound influence on the zeta potential of the silicon nitride surface [109], where the oxidized nitride surface might resist bacterial colonization due to its extreme negative surface charge. Li et al. [3] designed a DNA detection system based on DNA–PNA hybridization inside a microchannel, measured with a streaming potential analyzer, and obtained a detection limit of 10 nM. Yu et al. [114] developed a self-powered urea sensor by immobilizing catalytic enzymes on the microfluidic channel. The fluid pH increased when hydrolyzing urea into ions, which changed the measured streaming current.

In order to characterize the zeta potential of particles, the immobilization of particles into a substrate is required. Adamczyk et al. [113] covered mica with monodisperse latex particles, and measured the streaming potential with the addition of different salt solutions. Figure 5c shows the AFM image of latex particle monolayers on mica, and the reduction in the zeta potential of the surface at increased MgCl_2 ionic strength. Another way to measure the zeta potential of particles is to pack particles inside a plug, then measure the streaming potential by the flow of liquids through the plug [115]. Figure 5d shows the design for such a device, for detecting hydroxyapatite particles and the zeta potential relation, with a KCl concentration [115].

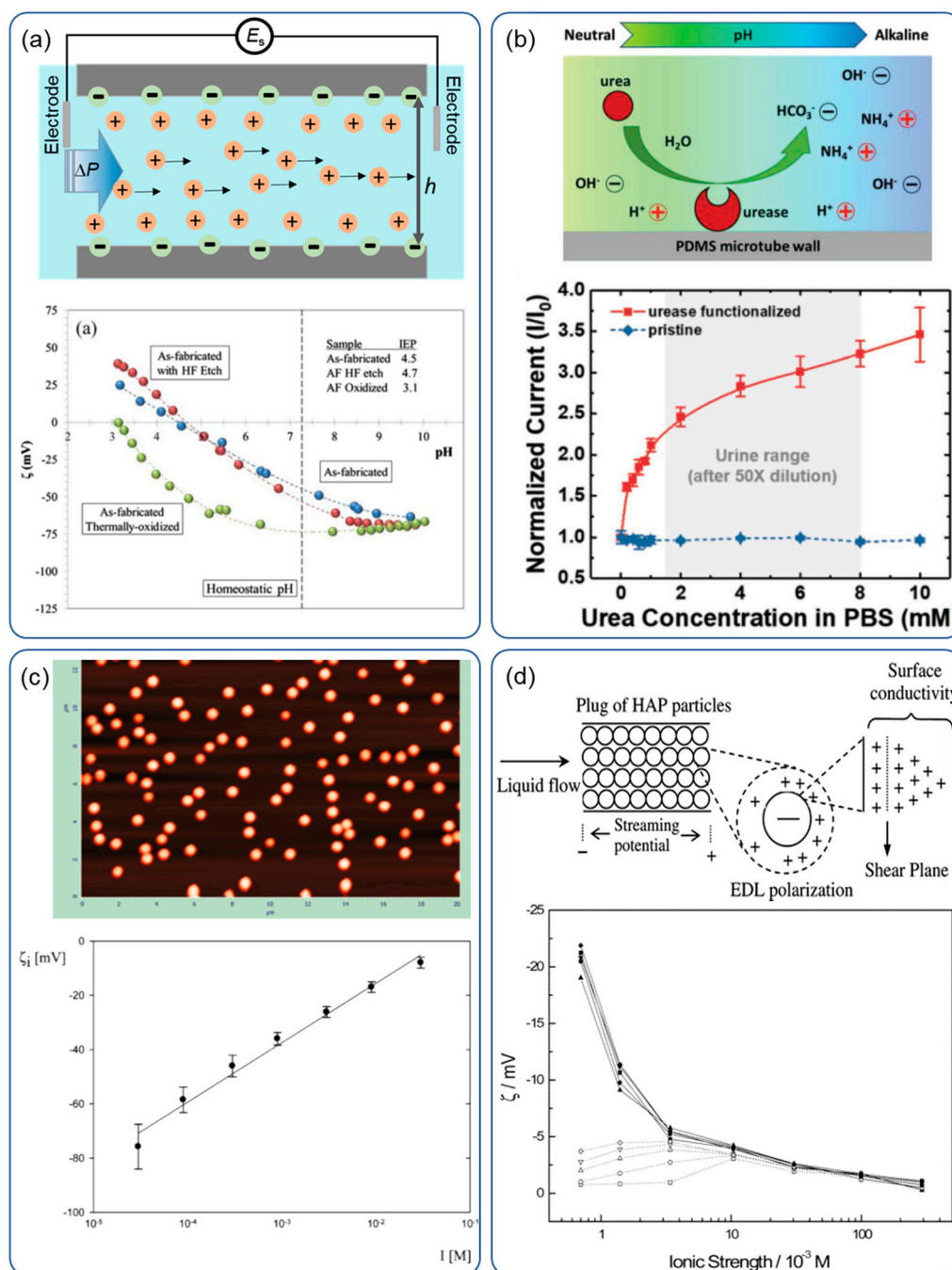


Figure 5. Streaming potential/current measurement for different applications. (a) A schematic setup (top) and characterization of surface treatment to silicon nitride surface (bottom) [109]; (b) schematic of urea hydrolysis catalyzed by the urease immobilized on microtube wall (top), and current output increases with increasing urea concentration from 0.0–10.0 mM (red line). The current output is independent of urea concentration without urea (blue line) [114]; (c) AFM (scan width 20 μ m) of latex particle monolayers on mica (top), and the zeta potential at different $MgCl_2$ concentration (bottom) [113]; (d) schematic diagram of a plug for detecting hydroxyapatite particles with flow potential (top), and relationship between the zeta potential and KCl ion concentrations (bottom) [115].

4.2. Optical Detection

Besides the streaming potential method, the zeta potential of particles can also be measured indirectly through electrophoretic motion [116], where electrophoretic light scattering (ELS), acoustics

and electroacoustics are commonly used methods. Among the three methods, ELS is commonly chosen for many applications due to its sensitivity, accuracy and versatility [117,118] in determining the zeta potential of suspended particles. However, the classic ELS uses transmitted light and receives scattering at a small angle (typically 8° – 30°), so it cannot be used for turbid samples because incident light cannot penetrate the sample [103].

Since molecules and particles are electrophoretic under the action of an applied electric field, their velocity is directly related to the amount of charge, and can be measured using laser coherence technology—specifically, the phase analysis light scattering method (M3-PALS). Figure 6a,b show a typical setup [119], where the laser beam is divided into a reference beam and an excitation beam. The excitation beam passes through the sample and the electric field is applied to induce particle electrophoresis. Moving particles scatter incident laser light, which causes a frequency shift from the excitation laser. The frequency shift is proportional to the speed of the particles, which is called Doppler shift [120]. The frequency difference is then measured by the ELS detector. According to Henry's equation and the light scattering Doppler shift theory, the zeta potential ζ of the particles can be calculated with [99]:

$$\zeta = \frac{3\eta\lambda\Delta f}{4\epsilon EF(\kappa a) \sin\left(\frac{\theta}{2}\right)} \quad (2)$$

where λ is the wavelength of incident light, Δf is the Doppler frequency shift; ϵ is the dielectric constant of the dispersant; E is the electric field strength; n is the refractive index of the solution; $F(\kappa a)$ is the Henry function and $1/\kappa$ is the Debye length, a is the radius of spherical particles; η is the viscosity; θ is the scattering angle.

The advantages of measuring zeta potential with ELS include minimal sample preparation, the analysis of large numbers of particles to provide good statistical results, and the use of disposable capillaries to prevent cross-contamination between samples. However, ELS is only suitable for uniform samples made with materials with the same optical characteristics [121]. Sample concentration also has a significant impact on the zeta potential measured with ELS [122]. Low concentrations can greatly reduce the signal-to-noise ratio and cause noisy and inconsistent results. In the contrary, high concentrations cause multiple scattering effects and particle interactions [98]. The optical configuration used in a typical laser Doppler instrument (such as Zetasizer Nano) calls for an optically transparent sample [99]. Therefore, in order to accurately measure the zeta potential, it is often necessary to dilute samples to reduce scattering. Another solution is to use unique electrodes that are conductive but transparent to incident and scattered light, which renders a shorter optical path length at a smaller scattering angle (about 35°), so as to avoid the interference of Brownian expansion [103]. One other way to measure the electrophoretic mobility of samples with a higher concentration is to reduce the path length of the cells, which increases the transmittance of the laser through the sample. Although such a cell can perform electrophoretic mobility measurements on a concentrated sample, the conversion to a zeta potential and subsequent interpretation of the obtained data is not easy. Kaszuba et al. [99] discussed electrophoretic mobility measurements on a high-concentration turbid sample with a new shortened cell, and found that, for the two sample types studied (titanium dioxide and polyurethane dispersion), the electrophoretic mobility showed a gradual decrease with increasing sample concentration.

Both nanoparticles and microparticles can be used for the zeta potential analysis of their surface modification [123]. Figure 6b shows the zeta potential difference for the amino, carboxyl and poly(ethylene glycol) functionalized surface. Furthermore, this can also be used to monitor the formation of nanoparticles with protein [126]. Based on such a mechanism, Wang et al. [124] presented biomolecular conjugated gold nanoparticles for ultra-sensitive protein quantification, as shown in Figure 6c. Bovine serum albumin on gold nanoparticles obtained a single-molecule resolution. Ma et al. [125] proposed a zeta potential sensing mechanism based on the electrostatic attraction of melamine and the formation of an N–Hg²⁺–N structure for the gold nanoparticles in the presence of

Hg^{2+} ions. Figure 6d outlines the sensing mechanism and the measured results. The decrease in negative charge on cysteamine-modified gold nanoparticles indicates the tendency of Hg^{2+} -caused aggregation.

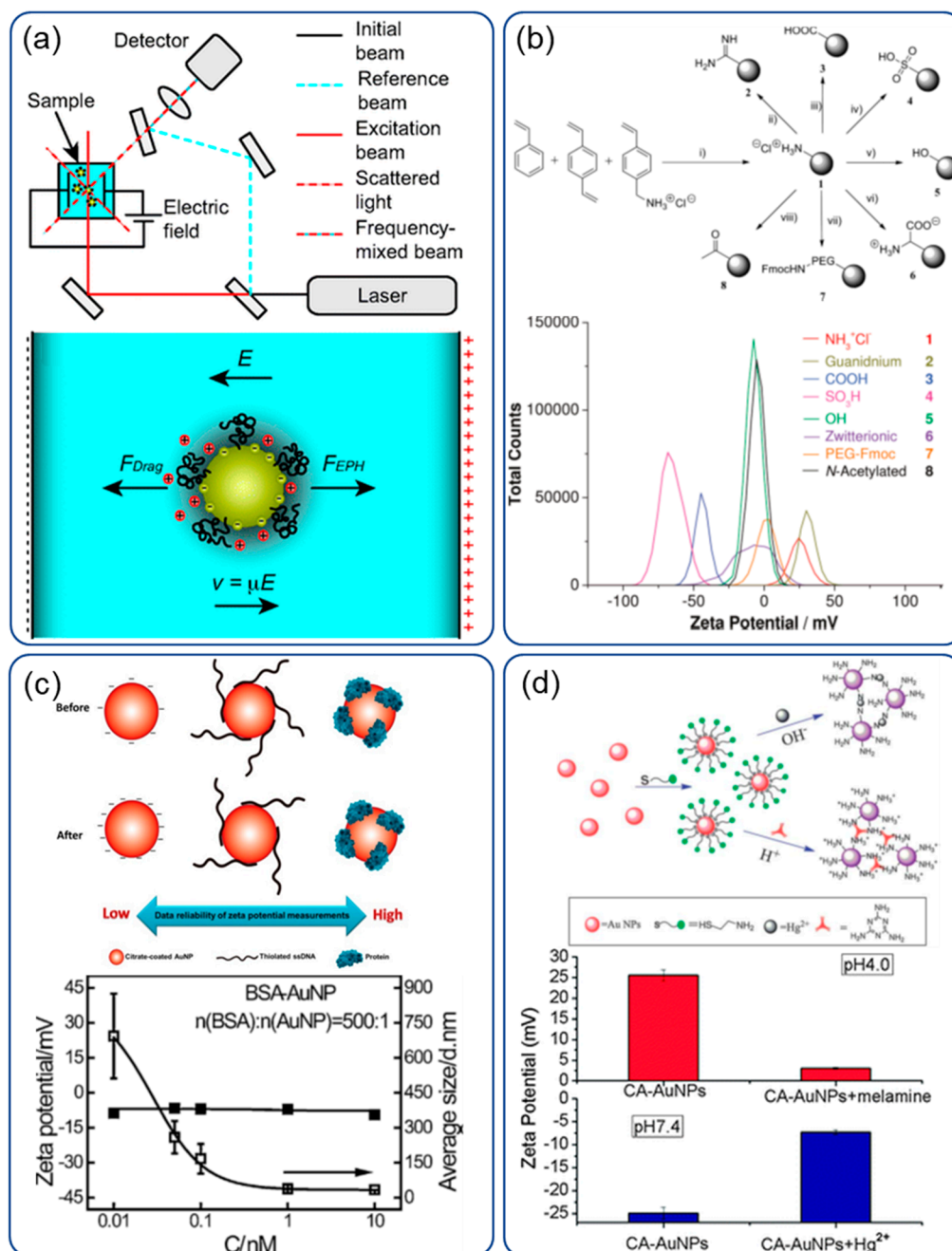


Figure 6. Electrophoretic light scattering for zeta potential measurements: (a) the light path for the detection system and the force analysis of particles under detection [119]; (b) zeta potential difference for various surface chemistries, e.g., amino, carboxyl and poly(ethylene glycol) and so on [123]; (c) bovine serum protein detection with AuNPs [124]; (d) surface chemistry for Hg^{2+} ion detection and a resultant reduction in zeta potential for Hg^{2+} ion adsorption [125].

5. Conclusions and Outlook

In this review, we summarized the surface potential/charge measurement techniques for monitoring the electric status of macroscopic planes and micro/nanoparticles, for applications in surface characterization, metal ion and biomolecule sensing. The detection mechanisms are discussed with optimization strategies. Both surface chemistries and sensing mechanisms have significant impacts

on the sensitivity. The presence of nanosensors, e.g., nanowires and nanopores, bring versatility, but also new challenges. Table 1 shows a comparison between the different detection techniques.

Table 1. Comparison of surface potential/charge detection techniques.

Detection Technique	KFM	ChemFET	Nanopore	Streaming Potential	Optical
Measurand	Surface potential	Surface potential	Surface charge	ζ -potential	ζ -potential
Detection signal	Potential difference	Current	Ionic current	Streaming potential/current	Frequency shift
Detection conditions	Non-conducting liquid and air	Both liquid and air	Low bulk conductivity liquid	Low bulk conductivity liquid	Liquid
Sensitivity	5 mV	1.5 mV	-	Sub-mV	Sub-mV
Portability	Non portable	Minimizable	Minimizable	Non portable	Portable
Application	Localized surface potential characterization; Ion detection; Biomolecule detection	Ion sensing; Biomolecule sensing; Cellular potential detection; Gas sensing	Ion sensing; Biomolecule detection; Gas sensing	Surface characterization; Ion sensing; Biomolecule detection	Ion sensing; Biomolecule detection;
Pros and cons	Sub-nm spatial resolution; Time consuming	nm scale resolution; Fast	Difficult signal conversion to surface charge; Fast	Wide applications; Medium speed	Minimal sample preparation; Require uniform sample; Fast
References	[22,33–40]	[51–67,75]	[83–95]	[107–115]	[116–124]

Further optimization of sensing techniques should focus on improving the sensitivity through the surface chemistry, sensing technique and analyzing method. Surface functionalization not only offers opportunities for a variety of targets, but also for complicated detection environments, e.g., direct measurements in serum with ISFET and protein blocking layers [59]. Finally, the combination of multiple techniques could benefit each other and offer robust and reliable methods to validate reactions [62,126]. We hope this review will provide cross-learning and new ideas for the development and applications of surface potential/charge detection techniques.

Author Contributions: Conceptualization, S.C.; writing and revision, S.C., H.D., J.Y. All authors have read and agreed to the published version of the manuscript.

Funding: This work was supported by the National Natural Science Foundation of China (Grant No. 61601387), the Natural Science Foundation of Fujian Province of China (Grant No. 2017J05107), the Open Funding of State Key Laboratory of Precision Measuring Technology and Instruments (Grant No. pilab1709), and the Guangdong Provincial Key laboratory of Optical Information Materials and Technology (Grant No. 2017B030301007).

Conflicts of Interest: The authors declare no conflict of interest.

References

1. Fu, W.; Jiang, L.; Van Geest, E.P.; Schneider, G.F.; Schneider, G.F. Sensing at the Surface of Graphene Field-Effect Transistors. *Adv. Mater.* **2016**, *29*, 1603610. [[CrossRef](#)] [[PubMed](#)]
2. Chen, S.; Tang, Y.; Zhan, K.; Sun, D.; Hou, X. Chemiresistive nanosensors with convex/concave structures. *Nano Today* **2018**, *20*, 84–100. [[CrossRef](#)]

3. Li, Y.; Lai, S.N.; Zheng, B. A microfluidic streaming potential analyzer for label-free DNA detection. *Sens. Actuators B Chem.* **2018**, *259*, 871–877. [[CrossRef](#)]
4. Chen, F.; Huang, H.; Guo, L.; Zhang, Y.; Ma, T. The Role of Polarization in Photocatalysis. *Angew. Chem. Int. Ed.* **2019**, *58*, 10061–10073. [[CrossRef](#)]
5. Takadoum, J. The influence of potential on the tribocorrosion of nickel and iron in sulfuric acid solution. *Corros. Sci.* **1996**, *38*, 643–654. [[CrossRef](#)]
6. Nordt, F.J. Alterations in surface charge density versus changes in surface charge topography in aging red blood cells. *Ann. Hematol.* **1980**, *40*, 233–238. [[CrossRef](#)]
7. Kirby, B.; Wheeler, A.R.; Zare, R.N.; Fruetel, J.A.; Shepodd, T.J. Programmable modification of cell adhesion and zeta potential in silica microchips. *Lab Chip* **2003**, *3*, 5–10. [[CrossRef](#)]
8. Zhu, X.; Mason, T.G. Separating Nanoparticles by Surface Charge Group Using pH-Controlled Passivated Gel Electrophoresis. *Soft Mater.* **2016**, *14*, 204–209. [[CrossRef](#)]
9. Chen, S.-L.; Wang, S.; Lucia, L.A. New insights into the fundamental nature of lignocellulosic fiber surface charge. *J. Colloid Interface Sci.* **2004**, *275*, 392–397. [[CrossRef](#)]
10. Salvo, P.; Melai, B.; Calisi, N.; Paoletti, C.; Bellagambi, F.G.; Kirchhain, A.; Trivella, M.; Fuoco, R.; Di Francesco, F. Graphene-based devices for measuring pH. *Sens. Actuators B Chem.* **2018**, *256*, 976–991. [[CrossRef](#)]
11. Ma, Y.; Yeh, L.-H.; Qian, S. pH-regulated ionic conductance in a nanopore. *Electrochem. Commun.* **2014**, *43*, 91–94. [[CrossRef](#)]
12. Cui, Y.; Wei, Q.; Park, H.; Lieber, C.M. Nanowire Nanosensors for Highly Sensitive and Selective Detection of Biological and Chemical Species. *Science* **2001**, *293*, 1289–1292. [[CrossRef](#)] [[PubMed](#)]
13. Lin, C.-Y.; Acar, E.T.; Polster, J.W.; Lin, K.; Hsu, J.-P.; Siwy, Z.S. Modulation of Charge Density and Charge Polarity of Nanopore Wall by Salt Gradient and Voltage. *ACS Nano* **2019**, *13*, 9868–9879. [[CrossRef](#)] [[PubMed](#)]
14. Chen, S.; Van Nieuwkastele, J.W.; Berg, A.V.D.; Eijkel, J. Ion-Step Method for Surface Potential Sensing of Silicon Nanowires. *Anal. Chem.* **2016**, *88*, 7890–7893. [[CrossRef](#)]
15. Kurkina, T.; Vlandas, A.; Ahmad, A.; Kern, K.; Balasubramanian, K. Label-Free Detection of Few Copies of DNA with Carbon Nanotube Impedance Biosensors. *Angew. Chem. Int. Ed.* **2011**, *50*, 3710–3714. [[CrossRef](#)]
16. Adam, T.; Hashim, U. Highly sensitive silicon nanowire biosensor with novel liquid gate control for detection of specific single-stranded DNA molecules. *Biosens. Bioelectron.* **2015**, *67*, 656–661. [[CrossRef](#)]
17. Chiesa, M.; Cardenas, P.; Otón, F.; Martínez, J.; Mas-Torrent, M.; Garcia, F.; Alonso, J.C.; Rovira, C.; Garcia, R. Detection of the Early Stage of Recombinational DNA Repair by Silicon Nanowire Transistors. *Nano Lett.* **2012**, *12*, 1275–1281. [[CrossRef](#)]
18. Duan, X.; Li, Y.; Rajan, N.K.; Routenberg, D.A.; Modis, Y.; Reed, M. Quantification of the affinities and kinetics of protein interactions using silicon nanowire biosensors. *Nat. Nanotechnol.* **2012**, *7*, 401–407. [[CrossRef](#)]
19. Chen, S.; Xie, Y.; De, A.; Berg, A.V.D.; Carlen, E.T. Electrical shielding for silicon nanowire biosensor in microchannels. *Appl. Phys. Lett.* **2013**, *103*, 173702. [[CrossRef](#)]
20. Kim, D.R.; Lee, C.H.; Zheng, X. Probing Flow Velocity with Silicon Nanowire Sensors. *Nano Lett.* **2009**, *9*, 1984–1988. [[CrossRef](#)]
21. Nonnenmacher, M.; O’Boyle, M.P.; Wickramasinghe, H. Kelvin probe force microscopy. *Appl. Phys. Lett.* **1991**, *58*, 2921–2923. [[CrossRef](#)]
22. Melitz, W.; Shen, J.; Kummel, A.; Lee, S. Kelvin probe force microscopy and its application. *Surf. Sci. Rep.* **2011**, *66*, 1–27. [[CrossRef](#)]
23. Arai, T.; Tomitori, M. Observation of electronic states on Si(111)-(7 × 7) through short-range attractive force with noncontact atomic force spectroscopy. *Phys. Rev. Lett.* **2004**, *93*, 256101. [[CrossRef](#)] [[PubMed](#)]
24. Okamoto, K.; Yoshimoto, K.; Sugawara, Y.; Morita, S. KPFM imaging of Si(1 1 1) 53 × 53 sb surface for atom distinction using NC-AFM. *Appl. Surf. Sci.* **2003**, *210*, 128–133. [[CrossRef](#)]
25. Shiota, T.; Nakayama, K. Atom-resolved imaging of the potential distribution at Si (111) 7 × 7 surfaces. *Jpn. J. Appl. Phys.* **2002**, *41*, L1178–L1180. [[CrossRef](#)]
26. Enevoldsen, G.H.; Glatzel, T.; Christensen, M.C.; Lauritsen, J.V.; Besenbacher, F. Atomic Scale Kelvin Probe Force Microscopy Studies of the Surface Potential Variations on the TiO₂(110) Surface. *Phys. Rev. Lett.* **2008**, *100*, 236104. [[CrossRef](#)]

27. Hoppe, H.; Glatzel, T.; Niggemann, M.; Hinsch, A.; Lux-Steiner, M.C.; Sariciftci, N.S. Kelvin Probe Force Microscopy Study on Conjugated Polymer/Fullerene Bulk Heterojunction Organic Solar Cells. *Nano Lett.* **2005**, *5*, 269–274. [[CrossRef](#)]
28. Hallam, T.; Duffy, C.M.; Minakata, T.; Ando, M.; Sirringhaus, H. A scanning Kelvin probe study of charge trapping in zone-cast pentacene thin film transistors. *Nanotechnology* **2008**, *20*, 025203. [[CrossRef](#)]
29. Clack, N.G.; Salaita, K.; Groves, J.T. Electrostatic readout of DNA microarrays with charged microspheres. *Nat. Biotechnol.* **2008**, *26*, 825–830. [[CrossRef](#)]
30. Stone, A.D.D.; Mesquida, P. Kelvin-probe force microscopy of the pH-dependent charge of functional groups. *Appl. Phys. Lett.* **2016**, *108*, 233702. [[CrossRef](#)]
31. García, R.; Garcia, R.; Pérez, R. Dynamic atomic force microscopy methods. *Surf. Sci. Rep.* **2002**, *47*, 197–301. [[CrossRef](#)]
32. Albrecht, T.R.; Horne, D.; Rugar, D.; Grütter, P. Frequency modulation detection using high-Q cantilevers for enhanced force microscope sensitivity. *J. Appl. Phys.* **1991**, *69*, 668–673. [[CrossRef](#)]
33. Ozasa, K.; Nemoto, S.; Maeda, M.; Hara, M. Kelvin probe force microscope with near-field photoexcitation. *J. Appl. Phys.* **2010**, *107*, 103501. [[CrossRef](#)]
34. Cohen, G.; Halpern, E.; Nanayakkara, S.U.; Luther, J.M.; Held, C.; Bennowitz, R.; Boag, A.; Rosenwaks, Y. Reconstruction of surface potential from Kelvin probe force microscopy images. *Nanotechnology* **2013**, *24*, 295702. [[CrossRef](#)] [[PubMed](#)]
35. Park, J.; Yang, J.; Lee, G.; Lee, C.Y.; Na, S.; Lee, S.W.; Haam, S.; Huh, Y.-M.; Yoon, D.S.; Eom, K.; et al. Single-Molecule Recognition of Biomolecular Interaction via Kelvin Probe Force Microscopy. *ACS Nano* **2011**, *5*, 6981–6990. [[CrossRef](#)]
36. Jang, K.; Choi, J.; Park, C.; Na, S. Label-free and high-sensitive detection of Kirsten rat sarcoma viral oncogene homolog and epidermal growth factor receptor mutation using Kelvin probe force microscopy. *Biosens. Bioelectron.* **2017**, *87*, 222–228. [[CrossRef](#)]
37. Leung, C.; Kinns, H.; Hoogenboom, B.W.; Howorka, S.; Mesquida, P. Imaging Surface Charges of Individual Biomolecules. *Nano Lett.* **2009**, *9*, 2769–2773. [[CrossRef](#)]
38. Park, C.; Jang, K.; Lee, S.; You, J.; Lee, S.; Ha, H.; Yun, K.; Kim, J.; Lee, H.; Park, J.; et al. A highly sensitive, direct and label-free technique for Hg²⁺ detection using Kelvin probe force microscopy. *Nanotechnology* **2015**, *26*, 305501. [[CrossRef](#)]
39. Park, J.; Lee, S.; Jang, K.; Na, S. Ultra-sensitive direct detection of silver ions via Kelvin probe force microscopy. *Biosens. Bioelectron.* **2014**, *60*, 299–304. [[CrossRef](#)]
40. Kim, W.; Lee, G.; Kim, M.; Park, J.; Jo, S.; Yoon, D.S.; Park, Y.H.; Hong, J.; Park, J. Al³⁺ ion sensing at attomole level via surface-potential mapping of gold nanoparticle complexes. *Sens. Actuators B Chem.* **2018**, *255*, 2179–2186. [[CrossRef](#)]
41. Luth, H. *Solid Surfaces, Interfaces and Thin Films*, 5th ed.; Springer: Berlin, Germany, 2010.
42. Sadewasser, S.; Leendertz, C.; Streicher, F.; Lux-Steiner, M.C. The influence of surface topography on Kelvin probe force microscopy. *Nanotechnology* **2009**, *20*, 505503. [[CrossRef](#)] [[PubMed](#)]
43. Garcia, R.; Herruzo, E.T. The emergence of multifrequency force microscopy. *Nat. Nanotechnol.* **2012**, *7*, 217–226. [[CrossRef](#)] [[PubMed](#)]
44. Ding, X.D.; An, J.; Xu, J.-B.; Li, C.; Zeng, R.Y. Improving lateral resolution of electrostatic force microscopy by multifrequency method under ambient conditions. *Appl. Phys. Lett.* **2009**, *94*, 223109. [[CrossRef](#)]
45. Stark, R.W.; Naujoks, N.; Stemmer, A. Multifrequency electrostatic force microscopy in the repulsive regime. *Nanotechnology* **2007**, *18*, 065502. [[CrossRef](#)]
46. Chen, S.; Bomer, J.G.; Van Der Wiel, W.G.; Carlen, E.T.; Berg, A.V.D. Top-Down Fabrication of Sub-30 nm Monocrystalline Silicon Nanowires Using Conventional Microfabrication. *ACS Nano* **2009**, *3*, 3485–3492. [[CrossRef](#)]
47. Elfström, N.; Karlström, A.E.; Linnros, J. Silicon Nanoribbons for Electrical Detection of Biomolecules. *Nano Lett.* **2008**, *8*, 945–949. [[CrossRef](#)]
48. Heller, I.; Janssens, A.M.; Männik, J.; Minot, E.D.; Lemay, S.G.; Dekker, C. Identifying the Mechanism of Biosensing with Carbon Nanotube Transistors. *Nano Lett.* **2008**, *8*, 591–595. [[CrossRef](#)]
49. Liao, L.; Bai, J.; Cheng, R.; Lin, Y.-C.; Jiang, S.; Huang, Y.; Duan, X. Top-Gated Graphene Nanoribbon Transistors with Ultrathin High-kDielectrics. *Nano Lett.* **2010**, *10*, 1917–1921. [[CrossRef](#)]

50. Vankerkhof, J.; Bergveld, P.; Schasfoort, R. The ISFET based heparin sensor with a monolayer of protamine as affinity ligand. *Biosens. Bioelectron.* **1995**, *10*, 269–282. [[CrossRef](#)]
51. Chen, S.; Bomer, J.G.; Carlen, E.T.; van den Berg, A. Al₂O₃/silicon nanoISFET with near ideal Nernstian response. *Nano Lett.* **2011**, *11*, 2334–2341. [[CrossRef](#)]
52. Heller, I.; Mannik, J.; Lemay, S.G.; Dekker, C. Optimizing the Signal-to-Noise Ratio for Biosensing with Carbon Nanotube Transistors. *Nano Lett.* **2009**, *9*, 377–382. [[CrossRef](#)] [[PubMed](#)]
53. Wipf, M.; Stoop, R.L.; Tarasov, A.; Bedner, K.; Fu, W.; Wright, I.A.; Martin, C.J.J.; Constable, E.C.; Calame, M.; Schönenberger, C.; et al. Selective Sodium Sensing with Gold-Coated Silicon Nanowire Field-Effect Transistors in a Differential Setup. *ACS Nano* **2013**, *7*, 5978–5983. [[CrossRef](#)] [[PubMed](#)]
54. Schasfoort, R.; Bergveld, P.; Kooyman, R.; Greve, J. The ion-step-induced response of membrane-coated ISFETs: Theoretical description and experimental verification. *Biosens. Bioelectron.* **1991**, *6*, 477–489. [[CrossRef](#)]
55. Novoselov, K.S.; Geim, A.K.; Morozov, S.V.; Jiang, D.; Katsnelson, M.I.; Grigorieva, I.V.; Dubonos, S.V.; Firsov, A.A. Two-dimensional gas of massless Dirac fermions in graphene. *Nature* **2005**, *438*, 197–200. [[CrossRef](#)]
56. Song, S.M.; Park, J.K.; Sul, O.J.; Cho, B.J. Determination of Work Function of Graphene under a Metal Electrode and Its Role in Contact Resistance. *Nano Lett.* **2012**, *12*, 3887–3892. [[CrossRef](#)] [[PubMed](#)]
57. Bergveld, P. Thirty years of isfetology—What happened in the past 30 years and what may happen in the next 30 years. *Sens. Actuators B Chem.* **2003**, *88*, 1–20. [[CrossRef](#)]
58. Kaisti, M. Detection principles of biological and chemical FET sensors. *Biosens. Bioelectron.* **2017**, *98*, 437–448. [[CrossRef](#)]
59. Park, S.; Kim, M.; Kim, D.; Kang, S.H.; Lee, K.H.; Jeong, Y. Interfacial charge regulation of protein blocking layers in transistor biosensor for direct measurement in serum. *Biosens. Bioelectron.* **2019**, *147*, 111737. [[CrossRef](#)]
60. Bhalla, N.; Di Lorenzo, M.; Pula, G.; Estrela, P. Protein phosphorylation analysis based on proton release detection: Potential tools for drug discovery. *Biosens. Bioelectron.* **2014**, *54*, 109–114. [[CrossRef](#)]
61. Gao, A.; Zou, N.; Dai, P.; Lu, N.; Li, T.; Wang, Y.; Zhao, J.; Mao, H. Signal-to-Noise Ratio Enhancement of Silicon Nanowires Biosensor with Rolling Circle Amplification. *Nano Lett.* **2013**, *13*, 4123–4130. [[CrossRef](#)]
62. Heerema, S.J.; Vicarelli, L.; Pud, S.; Schouten, R.N.; Zandbergen, H.W.; Dekker, C. Probing DNA Translocations with Inplane Current Signals in a Graphene Nanoribbon with a Nanopore. *ACS Nano* **2018**, *12*, 2623–2633. [[CrossRef](#)] [[PubMed](#)]
63. Cohen-Karni, T.; Qing, Q.; Li, Q.; Fang, Y.; Lieber, C.M. Graphene and Nanowire Transistors for Cellular Interfaces and Electrical Recording. *Nano Lett.* **2010**, *10*, 1098–1102. [[CrossRef](#)] [[PubMed](#)]
64. Patolsky, F.; Timko, B.; Yu, G.; Fang, Y.; Greytak, A.B.; Zheng, G.; Lieber, C.M. Detection, Stimulation, and Inhibition of Neuronal Signals with High-Density Nanowire Transistor Arrays. *Science* **2006**, *313*, 1100–1104. [[CrossRef](#)] [[PubMed](#)]
65. Tian, B.; Cohen-Karni, T.; Qing, Q.; Duan, X.; Xie, P.; Lieber, C.M. Three-Dimensional, Flexible Nanoscale Field-Effect Transistors as Localized Bioprobes. *Science* **2010**, *329*, 830–834. [[CrossRef](#)]
66. Zheng, G.; Patolsky, F.; Cui, Y.; Wang, W.U.; Lieber, C.M. Multiplexed electrical detection of cancer markers with nanowire sensor arrays. *Nat. Biotechnol.* **2005**, *23*, 1294–1301. [[CrossRef](#)]
67. Zou, X.; Wang, J.; Liu, X.; Wang, C.; Jiang, Y.; Wang, Y.; Xiao, X.; Ho, J.C.; Li, J.; Jiang, C.; et al. Rational Design of Sub-Parts per Million Specific Gas Sensors Array Based on Metal Nanoparticles Decorated Nanowire Enhancement-Mode Transistors. *Nano Lett.* **2013**, *13*, 3287–3292. [[CrossRef](#)]
68. Nair, P.R.; Alam, M.A. Design Considerations of Silicon Nanowire Biosensors. *IEEE Trans. Electron. Devices* **2007**, *54*, 3400–3408. [[CrossRef](#)]
69. Rajan, N.K.; Brower, K.; Duan, X.; Reed, M.A. Limit of detection of field effect transistor biosensors: Effects of surface modification and size dependence. *Appl. Phys. Lett.* **2014**, *104*, 084106. [[CrossRef](#)]
70. Tarasov, A.; Fu, W.; Knopfmacher, O.; Brunner, J.; Calame, M.; Schönenberger, C. Signal-to-noise ratio in dual-gated silicon nanoribbon field-effect sensors. *Appl. Phys. Lett.* **2011**, *98*, 12114. [[CrossRef](#)]
71. Dorvel, B.R.; Reddy, B.; Go, J.; Guevara, C.D.; Salm, E.; Alam, M.A.; Bashir, R. Silicon Nanowires with High-k Hafnium Oxide Dielectrics for Sensitive Detection of Small Nucleic Acid Oligomers. *ACS Nano* **2012**, *6*, 6150–6164. [[CrossRef](#)]

72. Nair, P.R.; Alam, M.A. Screening-Limited Response of NanoBiosensors. *Nano Lett.* **2008**, *8*, 1281–1285. [[CrossRef](#)] [[PubMed](#)]
73. Haight, R.; Sekaric, L.; Afzali, A.; Newns, D. Controlling the Electronic Properties of Silicon Nanowires with Functional Molecular Groups. *Nano Lett.* **2009**, *9*, 3165–3170. [[CrossRef](#)] [[PubMed](#)]
74. Park, C.W.; Ahn, C.-G.; Yang, J.-H.; Baek, I.-B.; Ah, C.S.; Kim, A.; Kim, T.-Y.; Sung, G.Y. Control of channel doping concentration for enhancing the sensitivity of ‘top-down’ fabricated Si nanochannel FET biosensors. *Nanotechnology* **2009**, *20*, 475501. [[CrossRef](#)] [[PubMed](#)]
75. Chen, S.; Berg, A.V.D.; Carlen, E.T. Sensitivity and detection limit analysis of silicon nanowire bio(chemical) sensors. *Sens. Actuators B Chem.* **2015**, *209*, 486–489. [[CrossRef](#)]
76. Pud, S.; Li, J.; Sibilliev, V.; Petrychuk, M.; Kovalenko, V.; Offenhäusser, A.; Vitusevich, S. Liquid and Back Gate Coupling Effect: Toward Biosensing with Lowest Detection Limit. *Nano Lett.* **2014**, *14*, 578–584. [[CrossRef](#)] [[PubMed](#)]
77. Gao, N.; Zhou, W.; Jiang, X.; Hong, G.; Fu, T.-M.; Lieber, C.M. General Strategy for Biodetection in High Ionic Strength Solutions Using Transistor-Based Nanoelectronic Sensors. *Nano Lett.* **2015**, *15*, 2143–2148. [[CrossRef](#)] [[PubMed](#)]
78. Masood, M.N.; Chen, S.; Carlen, E.T.; Berg, A.V.D. All-(111) Surface Silicon Nanowires: Selective Functionalization for Biosensing Applications. *ACS Appl. Mater. Interfaces* **2010**, *2*, 3422–3428. [[CrossRef](#)]
79. Zhang, G.-J.; Zhang, G.; Chua, J.H.; Chee, R.-E.; Wong, E.-H.; Agarwal, A.; Buddharaju, K.D.; Singh, N.; Gao, Z.; Balasubramanian, N. DNA Sensing by Silicon Nanowire: Charge Layer Distance Dependence. *Nano Lett.* **2008**, *8*, 1066–1070. [[CrossRef](#)]
80. Elnathan, R.; Kwiat, M.; Pevzner, A.; Engel, Y.; Burstein, L.; Khatchourints, A.; Lichtenstein, A.; Kantsev, R.; Patolsky, F. Biorecognition Layer Engineering: Overcoming Screening Limitations of Nanowire-Based FET Devices. *Nano Lett.* **2012**, *12*, 5245–5254. [[CrossRef](#)]
81. Bhattacharyya, I.M.; Shalev, G. Electrostatically Governed Debye Screening Length at the Solution-Solid Interface for Biosensing Applications. *ACS Sens.* **2020**, *5*, 154–161. [[CrossRef](#)]
82. Tang, Y.; Cao, L.; Zhan, K.; Xie, Y.; Sun, D.; Hou, X.; Chen, S. Performance analysis of solid-state nanopore chemical sensor. *Sens. Actuators B Chem.* **2019**, *286*, 315–320. [[CrossRef](#)]
83. Ali, M.; Ramírez, P.; Mafe, S.; Neumann, R.; Ensinger, W. A pH-Tunable Nanofluidic Diode with a Broad Range of Rectifying Properties. *ACS Nano* **2009**, *3*, 603–608. [[CrossRef](#)] [[PubMed](#)]
84. Ramirez, P.; Manzanares, J.A.; Cervera, J.; Gomez, V.; Ali, M.; Nasir, S.; Ensinger, W.; Mafe, S. Surface charge regulation of functionalized conical nanopore conductance by divalent cations and anions. *Electrochim. Acta* **2019**, *325*, 134914. [[CrossRef](#)]
85. Lucas, R.A.; Lin, C.-Y.; Siwy, Z.S. Electrokinetic Phenomena in Organic Solvents. *J. Phys. Chem. B* **2019**, *123*, 6123–6131. [[CrossRef](#)]
86. Wang, R.; Sun, Y.; Zhang, F.; Song, M.; Tian, D.; Li, H. Temperature-Sensitive Artificial Channels through Pillar [5] arene-based Host-Guest Interactions. *Angew. Chem. Int. Ed.* **2017**, *56*, 5294–5298. [[CrossRef](#)]
87. Pérez-Mitta, G.; Peinetti, A.S.; Cortez, M.L.; Toimil-Molares, M.E.; Trautmann, C.; Azzaroni, O. Highly Sensitive Biosensing with Solid-State Nanopores Displaying Enzymatically Reconfigurable Rectification Properties. *Nano Lett.* **2018**, *18*, 3303–3310. [[CrossRef](#)]
88. Xu, Y.; Sui, X.; Guan, S.; Zhai, J.; Gao, L. Olfactory Sensory Neuron-Mimetic CO₂ Activated Nanofluidic Diode with Fast Response Rate. *Adv. Mater.* **2015**, *27*, 1851–1855. [[CrossRef](#)]
89. Schoch, R.B.; Renaud, P. Ion transport through nanoslits dominated by the effective surface charge. *Appl. Phys. Lett.* **2005**, *86*, 253111. [[CrossRef](#)]
90. Pérez-Mitta, G.; Albesa, A.G.; Knoll, W.; Trautmann, C.; Toimil-Molares, M.E.; Azzaroni, O. Host-guest supramolecular chemistry in solid-state nanopores: Potassium-driven modulation of ionic transport in nanofluidic diodes. *Nanoscale* **2015**, *7*, 15594–15598. [[CrossRef](#)]
91. Gao, R.; Ying, Y.-L.; Yan, B.-Y.; Iqbal, P.; Preece, J.A.; Wu, X. Ultrasensitive determination of mercury(II) using glass nanopores functionalized with macrocyclic dioxotetraamines. *Microchim. Acta* **2015**, *183*, 491–495. [[CrossRef](#)]
92. Chen, L.; He, H.; Xu, X.; Jin, Y. Single glass nanopore-based regenerable sensing platforms with a non-immobilized polyglutamic acid probe for selective detection of cupric ions. *Anal. Chim. Acta* **2015**, *889*, 98–105. [[CrossRef](#)] [[PubMed](#)]

93. Ali, M.; Neumann, R.; Ensinger, W. Sequence-Specific Recognition of DNA Oligomer Using Peptide Nucleic Acid (PNA)-Modified Synthetic Ion Channels: PNA/DNA Hybridization in Nanoconfined Environment. *ACS Nano* **2010**, *4*, 7267–7274. [[CrossRef](#)] [[PubMed](#)]
94. Cai, S.-L.; Cao, S.-H.; Zheng, Y.-B.; Zhao, S.; Yang, J.-L.; Li, Y. Surface charge modulated aptasensor in a single glass conical nanopore. *Biosens. Bioelectron.* **2015**, *71*, 37–43. [[CrossRef](#)] [[PubMed](#)]
95. Mayne, L.; Lin, C.-Y.; Christie, S.; Siwy, Z.S.; Platt, M. The Design and Characterization of Multifunctional Aptamer Nanopore Sensors. *ACS Nano* **2018**, *12*, 4844–4852. [[CrossRef](#)] [[PubMed](#)]
96. Ma, Y.; Yeh, L.-H.; Lin, C.-Y.; Mei, L.; Qian, S. pH-Regulated Ionic Conductance in a Nanochannel with Overlapped Electric Double Layers. *Anal. Chem.* **2015**, *87*, 4508–4514. [[CrossRef](#)] [[PubMed](#)]
97. Mei, L.; Yeh, L.-H.; Qian, S. Buffer effect on the ionic conductance in a pH-regulated nanochannel. *Electrochem. Commun.* **2015**, *51*, 129–132. [[CrossRef](#)]
98. Clogston, J.D.; Patri, A.K. Zeta Potential Measurement. *Adv. Struct. Saf. Stud.* **2010**, *697*, 63–70.
99. Kaszuba, M.; Corbett, J.; Watson, F.M.; Jones, A. High-concentration zeta potential measurements using light-scattering techniques. *Philos. Trans. R. Soc. A Math. Phys. Eng. Sci.* **2010**, *368*, 4439–4451. [[CrossRef](#)]
100. Lyklema, J. Electrokinetics after Smoluchowski. *Colloids Surf. A Physicochem. Eng. Asp.* **2003**, *222*, 5–14. [[CrossRef](#)]
101. Vinogradov, J.; Jackson, M.; Chamerois, M. Zeta potential in sandpacks: Effect of temperature, electrolyte pH, ionic strength and divalent cations. *Colloids Surf. A Physicochem. Eng. Asp.* **2018**, *553*, 259–271. [[CrossRef](#)]
102. Gittings, M.; Saville, D. The determination of hydrodynamic size and zeta potential from electrophoretic mobility and light scattering measurements. *Colloids Surf. A Physicochem. Eng. Asp.* **1998**, *141*, 111–117. [[CrossRef](#)]
103. Xu, R. Progress in nanoparticles characterization: Sizing and zeta potential measurement. *Particuology* **2008**, *6*, 112–115. [[CrossRef](#)]
104. Shin, S.; Ault, J.; Feng, J.; Warren, P.B.; Stone, H.A. Low-Cost Zeta Potentiometry Using Solute Gradients. *Adv. Mater.* **2017**, *29*, 1701516. [[CrossRef](#)] [[PubMed](#)]
105. Delgado, A.; Caballero, F.G.; Hunter, R.; Koopal, L.; Lyklema, J. Measurement and interpretation of electrokinetic phenomena. *J. Colloid Interface Sci.* **2007**, *309*, 194–224. [[CrossRef](#)] [[PubMed](#)]
106. Voigt, A.; Wolf, H.; Lauekner, S.; Neumann, G.; Becker, R.; Richter, L. Electrokinetic properties of polymer and glass surfaces in aqueous solutions: Experimental evidence for swollen surface layers. *Biomaterials* **1983**, *4*, 299–304. [[CrossRef](#)]
107. Sze, A.; Erickson, D.; Ren, L.; Li, N. Zeta-potential measurement using the Smoluchowski equation and the slope of the current–time relationship in electroosmotic flow. *J. Colloid Interface Sci.* **2003**, *261*, 402–410. [[CrossRef](#)]
108. Glad, C.; Sjödin, K.; Mattiasson, B. Streaming potential—A general affinity sensor. *Biosensors* **1986**, *2*, 89–100. [[CrossRef](#)]
109. Bock, R.M.; McEntire, B.J.; Bal, B.S.; Rahaman, M.N.; Boffelli, M.; Pezzotti, G. Surface modulation of silicon nitride ceramics for orthopaedic applications. *Acta Biomater.* **2015**, *26*, 318–330. [[CrossRef](#)]
110. Childress, A.E.; Elimelech, M. Relating Nanofiltration Membrane Performance to Membrane Charge (Electrokinetic) Characteristics. *Environ. Sci. Technol.* **2000**, *34*, 3710–3716. [[CrossRef](#)]
111. Muff, L.F.; Luxbacher, T.; Burgert, I.; Michen, B. Investigating the time-dependent zeta potential of wood surfaces. *J. Colloid Interface Sci.* **2018**, *518*, 165–173. [[CrossRef](#)]
112. Pusić, T.; Grancarić, A.M.; Soljačić, I.; Ribitsch, V. The effect of mercerisation on the electrokinetic potential of cotton. *Color. Technol.* **1999**, *115*, 121–124. [[CrossRef](#)]
113. Adamczyk, Z.; Zaucha, M.; Zembala, M. Zeta Potential of Mica Covered by Colloid Particles: A Streaming Potential Study. *Langmuir* **2010**, *26*, 9368–9377. [[CrossRef](#)] [[PubMed](#)]
114. Yu, L.; Shi, C.; Xi, W.; Yeo, J.C.; Soon, R.H.; Chen, Z.; Song, P.; Lim, C.T. Streaming Current Based Microtubular Enzymatic Sensor for Self-Powered Detection of Urea. *Adv. Mater. Technol.* **2018**, *4*, 1800430. [[CrossRef](#)]
115. Skartsila, K.; Spanos, N. Physicochemical Characterization of Various Packed Porous Plugs of Hydroxyapatite: Streaming Potential Coupled with Conductivity Measurements. *Langmuir* **2006**, *22*, 1903–1910. [[CrossRef](#)]
116. Thomas, J.C.; Hanton, K.L.; Crosby, B.J. Measurement of the Field Dependent Electrophoretic Mobility of Surface Modified Silica/AOT Suspensions. *Langmuir* **2008**, *24*, 10698–10701. [[CrossRef](#)]
117. Xu, R.; Smart, G. Electrophoretic Mobility Study of Dodecyltrimethylammonium Bromide in Aqueous Solution and Adsorption on Microspheres. *Langmuir* **1996**, *12*, 4125–4133. [[CrossRef](#)]

118. Xu, R.; Wu, C.; Xu, H. Particle size and zeta potential of carbon black in liquid media. *Carbon* **2007**, *45*, 2806–2809. [[CrossRef](#)]
119. Doane, T.L.; Chuang, C.H.; Hill, R.J.; Burda, C. Nanoparticle zeta-potentials. *Acc. Chem. Res.* **2012**, *45*, 317–326. [[CrossRef](#)]
120. Bhattacharjee, S. DLS and zeta potential—What they are and what they are not? *J. Control. Release* **2016**, *235*, 337–351. [[CrossRef](#)]
121. Tantra, R.; Schulze, P.; Quincey, P. Effect of nanoparticle concentration on zeta-potential measurement results and reproducibility. *Particuology* **2010**, *8*, 279–285. [[CrossRef](#)]
122. Thielbeer, F.; Donaldson, K.; Bradley, M. Zeta Potential Mediated Reaction Monitoring on Nano and Microparticles. *Bioconjugate Chem.* **2011**, *22*, 144–150. [[CrossRef](#)] [[PubMed](#)]
123. Wang, W.; Ding, X.; Xu, Q.; Wang, J.; Wang, L.; Lou, X. Zeta-potential data reliability of gold nanoparticle biomolecular conjugates and its application in sensitive quantification of surface absorbed protein. *Colloids Surf. B Biointerfaces* **2016**, *148*, 541–548. [[CrossRef](#)] [[PubMed](#)]
124. Ma, Y.; Jiang, L.; Mei, Y.; Song, R.; Tian, D.B.; Huang, H. Colorimetric sensing strategy for mercury(II) and melamine utilizing cysteamine-modified gold nanoparticles. *Analyst* **2013**, *138*, 5338–5348. [[CrossRef](#)] [[PubMed](#)]
125. Casals, E.; Pfaller, T.; Duschl, A.; Oostingh, G.J.; Puntès, V. Time Evolution of the Nanoparticle Protein Corona. *ACS Nano* **2010**, *4*, 3623–3632. [[CrossRef](#)] [[PubMed](#)]
126. Bhalla, N.; Formisano, N.; Miodek, A.; Jain, A.; Di Lorenzo, M.; Pula, G.; Estrela, P. Plasmonic ruler on field-effect devices for kinase drug discovery applications. *Biosens. Bioelectron.* **2015**, *71*, 121–128. [[CrossRef](#)] [[PubMed](#)]



© 2020 by the authors. Licensee MDPI, Basel, Switzerland. This article is an open access article distributed under the terms and conditions of the Creative Commons Attribution (CC BY) license (<http://creativecommons.org/licenses/by/4.0/>).